PCCP

Accepted Manuscript

ROYAL SOCIETY OF CHEMISTRY

www.rsc.org/pccp

Crystallographic transformation of limestone during calcination under CO_2

Jose Manuel Valverde[a], Santiago Medina[b]

[a] Faculty of Physics. University of Seville. Avenida Reina Mercedes s/n, 41012 Sevilla, Spain

[b] X-Ray Laboratory (CITIUS), University of Seville,

Avenida Reina Mercedes, 4B. 41012 Sevilla, Spain

Abstract

The calcination reaction of limestone ($CaCO_3$) to yield lime (CaO) is at the heart of many industrial applications as well as natural processes. In the recently emerged Calcium-looping technology, CO_2 capture is accomplished by the carbonation of CaO in a gas-solid reactor (carbonator). CaO is derived by calcination of limestone in a calciner reactor under necessarily high CO_2 partial pressure and high temperature. In-situ X-ray diffraction (XRD) is employed in this work to gain further insight on the crystallographic transformation that takes place during calcination of limestone under CO_2 at partial pressures P close to the equilibrium pressure P_{eq} and high temperature. Calcination under these conditions becomes extremely slow. The in-situ XRD analysis presented here suggests the presence of an intermediate metastable CaO^* phase stemming from the parent $CaCO_3$ structure. According to the reaction mechanism proposed elsewhere, the exothermicity of the $CaO^* \rightarrow CaO$ transformation and high values of P/P_{eq} inhibit the nucleation of CaO at high temperatures. The wt% of CaO^* remains at a relatively high level during slow calcination. Two diverse stages have been identified in the evolution of CaO crystallite size L. Initially, L is increased with $CaCO_3$ conversion following a logarithmic law. Slow calcination allows the crystallite size to grow up from a few nanometers at nucleation up to around 100 nm near the end of conversion. Otherwise, quick calcination at relatively lower CO_2 concentrations limits CaO crystallite growth. Once calcination reaches an advanced state, the presence of CaO^* drops to zero and the rate of increase of CaO crystallite size is significantly hindered. Arguably, the first stage in CaO crystallite growth is driven by aggregation of the metastable CaO^* nanocrystals as due to surface attractive forces whereas the second one obeys to sintering of the aggregated CaO crystals and persists with time after full calcination is attained. Our analysis shows that the main mechanism responsible for the

increase of CaO crystallite size (and thus for undermining the reactivity of CaO) under high CO_2 partial pressure is enhanced aggregation whereas CaO sintering is relatively less relevant as would be expected for calcination temperatures well below the Tamman temperature.

I. INTRODUCTION

Lime (CaO) is a main raw material used in a vast number of natural and industrial processes including cement, iron and steel, agriculture, food processing, disinfection, water treatment, desulphurization, plastics, glass, sugar refining and pharmaceutical among others. Thus, the calcination of limestone ($CaCO_3$)

$$CaCO_3 \leftrightarrows CaO + CO_2(g) \quad \Delta_r H^0 = +177.8\text{kJ/mol} \tag{1}$$

to obtain lime is probably the most frequently investigated reaction involving the decomposition of a solid reactant. Yet, a thorough understanding of the underlying physicochemical mechanisms that govern limestone calcination remains elusive [1–4]. The kinetics of calcination is mainly determined by the calcination temperature T, calcination atmosphere and $CaCO_3$ conversion degree α (defined as the ratio of mass of $CaCO_3$ calcined to the initial mass). At a given temperature T, the CO_2 partial pressure at equilibrium is given by

$$P_{eq}(\text{atm}) \approx 4.083 \times 10^7 \exp(-20474/T) \tag{2}$$

as inferred from thermochemical data [5–7]. If the CO_2 partial pressure in the calcination environment P is much smaller than P_{eq}, the rate of $CaCO_3$ conversion is essentially governed by the calcination temperature T and can be generally well fitted by an Arrhenius law [3, 4, 8]

$$\frac{d\alpha}{dt} = r(T,P)\, f(\alpha) \tag{3}$$

$$r(T,P) = A\, \exp(-E_1/RT) \left(1 - \frac{P}{P_{eq}}\right)^{\gamma} \tag{4}$$

where r is the surface reaction rate, $f(\alpha)$ is a mechanistic-rate function [9], A is a pre-exponential term, γ is an empirical exponent of order unity, $R = 8.3145$ J/mol-K is the ideal gas constant and E_1 is a positive activation energy, which is about the calcination enthalpy change $E_1 \approx \Delta_r H^0$ [10].

Experimental observations indicate that limestone calcination should occur through a crystallographic transformation involving a topotactical chemical decomposition of $CaCO_3$ yielding an intermediate metastable CaO^* phase that subsequently transforms into the stable CaO form [3, 11–16]. Accordingly, a reaction mechanism model has been recently proposed consisting of two steps [17, 18]:

1. **Chemical decomposition**

$$\mathrm{CaCO_3} + \underset{1-\phi}{L} \underset{k_2}{\overset{k_1}{\rightleftharpoons}} \underset{a^*}{\mathrm{CaO^*}} + \underset{\phi}{L(\mathrm{CO_2})}$$

2. **Desorption/structural transformation**

$$\underset{a^*}{\mathrm{CaO^*}} + \underset{\phi}{L(\mathrm{CO_2})} \underset{k_a}{\overset{k_d}{\rightleftharpoons}} \mathrm{CaO} + \underset{1-\phi}{L} + \underset{P}{\mathrm{CO_2}(g)}$$

Here L represents an active site in the solid where calcination occurs, $L(CO_2)$ denotes a molecule of CO_2 that remains physically adsorbed after chemical decomposition, ϕ is the fraction of active sites filled with adsorbed CO_2, k_i are the reaction rate constants and $a^* = \exp(\Delta G^*/RT)$ is the activity of the metastable CaO^* form [13], where $\Delta G^* = \Delta H^* - T\Delta S^* > 0$ is the free Gibbs energy of formation of the metastable oxide from the

stable form. Under the assumption that chemical decomposition is the rate-limiting step (k_1, $k_2 << k_d$, $k_a P$), the reaction rate predicted is [18]

$$r \approx r_1 = a_1 \exp(-E_1/RT)\left(1 - \frac{P}{P_{eq}}\right)(1-\phi) \quad (5)$$

$$1-\phi \approx \frac{1}{1+(K_1/a^*)P/P_{eq}} \quad (6)$$

where $K_1 = \exp(-\Delta_1 G^0/RT)$, $\Delta_1 G^0 = \Delta_1 H^0 - T\Delta_1 S^0 < 0$ is the standard free energy change of chemical decomposition and the rate constant k_1 is assumed to follow an Arrhenius law with an activation energy E_1 ($k_1 = a_1 \exp(-E_1/RT)$). In the limit of very low CO_2 partial pressure ($P/P_{eq} \ll 1$) and/or low temperatures ($K_1/a^* = \exp(-(\Delta_1 G^0 + \Delta G^*)/RT) \ll 1$), the fraction of active sites with adsorbed CO_2 molecules is negligible ($\phi \simeq 0$) and the reaction rate conforms to Eq. 4. On the other hand, for P/P_{eq} close to unity and high temperatures ($\exp(-(\Delta_1 G^0 + \Delta G^*)/RT)(P/P_{eq}) \gg 1$) it is $\phi \simeq 1 - \exp((\Delta_1 G^0 + \Delta G^*)/RT)(P_{eq}/P) \approx 1$. In this limiting situation CO_2 desorption is hindered and the reaction rate can be written as

$$r \approx a_1 A_1 A^* \exp(-E_{ap}/RT)\left(\frac{P_{eq}}{P} - 1\right) \quad (7)$$

where $A_1 = \exp(-\Delta_1 S^0/R)$, $A^* = \exp(-\Delta S^*/R)$ and $E_{ap} = E_1 - \Delta_1 H^0 - \Delta H^*$. The activation energy under these conditions E_{ap} would be negative since the structural transformation is exothermic ($-\Delta H^* < 0$ [16]) and the value of E_1 is expected on the order of the chemical decomposition enthalpy change $\Delta_1 H^0$. Thus, if P/P_{eq} is high, the reaction rate would conform to Eq. 4 with an activation energy $E_1 > 0$ only at low temperatures. As the temperature is increased, the activation energy would be decreased with temperature and turn to be negative above a certain critical temperature T_c. At temperatures above this

critical value, the reaction rate is markedly decreased with temperature and conforms to Eq. 7 in the high temperature limit as seen from thermogravimetric tests in a recent work [18]. The value of T_c increases as P/P_{eq} is decreased and for $P/P_{eq} < 0.6$, the reaction rate adjusts to Eq. 4 with a positive activation energy within the whole range of calcination temperatures usually employed in practice [18].

A. The Ca-looping technology for post-combustion CO_2 capture

The analysis of limestone calcination in environments of high CO_2 partial pressure has gained a great interest in the last years fueled by the recently emerged Ca-looping (CaL) technology for CO_2 capture from coal fired power plants [19–21]. The multicyclic calcination/carbonation of limestone is at the basis of this potentially low cost 2^{nd} generation capture technology. Lime particles undergo carbonation at contact with the flue gas in a fluidized bed at temperatures around 650°C after which the partially carbonated solids are circulated into a calciner for CaO regeneration at atmospheric pressure. The main goal of the process is to retrieve CO_2 as a highly concentrated stream from the calciner reactor. In order not to dilute CO_2 in the calciner reactor, the most suitable method for calcination at high temperatures is to burn coal in the calciner using O_2 (oxy-combustion). Yet, calcination under CO_2 at high partial pressure and high temperatures leads to a marked loss of CaO reactivity that makes it necessary to continuously feed the calciner with a fresh makeup flow of limestone while the deactivated sorbent is purged. According to Eq. 2, the minimum temperature for calcination in a pure CO_2 environment at atmospheric pressure ($P = 1$ atm) would be $T_{cal} \simeq 895$°C (P/P_{eq}=1). Both the carbonator and calciner employed in 1-2 MW_{th} pilot-scale tests [21, 22] and modeled in process simulations [20] are Circulating Fluidized Bed (CFB) reactors operated in the fast fluidization regime, which provides a high

heat/mass transfer efficiency for typically short residence times. Yet, the temperature in the calciner has to be increased over $T_{cal} \simeq 930°C$ (or, equivalently, P/P_{eq} decreased below $P/P_{eq} \simeq 0.6$) for calcination of the makeup flow of natural limestone to be fully achieved in a few minutes [21–27]. This imposes an important energy penalty to the technology since oxy-combustion requires the additional consumption of fuel and oxygen and generates additional CO_2 [24, 25, 28–30]. The purpose of the present work is to investigate the crystallographic transformation that takes place in the calcination reaction of natural limestone nearby equilibrium as affected by a high CO_2 concentration in the calciner environment. To this end, XR diffractograms (XRD) of limestone samples have been continuously recorded in-situ as the samples undergo calcination for a range of controlled values of P/P_{eq} and temperature. A quantitative analysis of the obtained results will serve to establish a link between the calcination kinetics and the details of the structural transformation.

II. EXPERIMENTAL MATERIAL AND METHODS

The material tested has been a powdered natural limestone of high purity (99.62% $CaCO_3$, $SiO_2 < 0.05\%$, $Al_2O_3 < 0.05\%$, 0.24% MgO, 0.08% Na_2O) from Matagallar quarry (Pedrera, Spain) with average particle size of 9.5 μm (volume weighted mean particle size) as measured by laser diffractometry using a Malvern Mastersizer 2000 instrument.

Figure 1 shows a schematic layout of the experimental setup used in our work. The powder sample of mass around 150 mg is placed over a 1 cm diameter porous ceramic plate. A N_2/CO_2 controlled gas mixture is passed at atmospheric pressure across the powder at a small flow rate (100 $cm^3 min^{-1}$). By distributing the gas across the sample layer, the gas-solid contacting efficiency is enhanced, which serves to minimize undesired effects of inefficient mass and heat transfer on the reaction rate. Likewise, the small size of the particles

allows us neglecting intra-particle diffusion resistance effects on the reaction rate that would be relevant only for particles of size larger than 300 μm [6, 31]. The powder diffractometer employed (Bruker D8 Advance) is equipped with an Anton Paar XRK 900 high temperature chamber wherein the sample is contained and a fast response/high sensitivity detector (Bruker Vantec 1) with radial Soller slits, which allows us to analyze the time evolution of the solid crystal structure as calcination progresses at controlled conditions of temperature and CO_2 partial pressure. The XRK 900 reactor chamber is specifically built for the kinetic analysis of gas-solid reactions up to high temperatures without any dead volumes to ensure homogeneous filling with the reaction gas. The entire set of sample and sample holder rests inside a furnace with a heater designed to guarantee the absence of temperature gradients across the sample. NiCr/NiAl thermocouples placed near the sample holder provide a reliable measurement and control of temperature. In-situ XRD tests were performed using 60 mm Gobel mirrors (Bruker, Germany) for Cu K_α radiation (0.15405 nm wavelength) and with parallel Johansson geometry in the incident beam. The diffractometer was calibrated mechanically following manufacturer specifications. Corundum, LaB_6 and silicon standards were employed to check resolution and to obtain instrumental contribution for structural adjustments in a wide range of diffraction angles.

In each test, the temperature is increased from ambient temperature at 12°C/min up to the target calcination temperature, which is kept constant while XRD scans are continuously recorded. The Cu K-α radiation interacts with the sample across a thickness of about 100μm, which is greater than particle size in our limestone powder. Thus, the XRD analysis is useful to obtain the time evolution of the $CaCO_3$/CaO weight fraction as calcination progresses. XRD scans of short duration (140 s) are continuously registerd in the range $17.5° < 2\theta < 39.5°$ (0.022°/step) to record the main Bragg peaks for calcite and lime with a sufficiently large

number of counts in order to analyze the reaction kinetics and the time evolution of the nascent CaO crystallite size. XRD scans were also carried out in a wider range of diffraction angles ($18° < 2\theta < 115°$) in order to carry out a quantitative phase Rietveld analysis aimed at identifying the presence of a metastable CaO^* phase during slow calcination as suggested elsewhere [3]. Calcination tests have been performed in a range of CO_2 vol.% between 5% and 100% and temperatures T between 730°C and 923°C as to yield data series at fixed ratios P/P_{eq} =0.6, 0.7, 0.8 and 0.9.

III. RESULTS AND DISCUSSION

A. Calcination kinetics

Figure 2 illustrates examples of XRD scans recorded during calcination tests in a range of temperatures 857°C $< T <$895°C and for $P/P_{eq} = 0.9$. In qualitative agreement with Eq. 7, the diffractograms show that the reaction is significantly hindered for a fixed and high value of P/P_{eq} as the calcination temperature is increased. The induction period that precedes the emergence of the CaO Bragg reflection peaks becomes also extraordinarily prolonged as the temperature is increased. Thus, for calcination at $T = 895$°C (90% CO_2 vol) the induction period lasts about 45 min and at $T = 903$°C (100% CO_2 vol, $P/P_{eq} = 0.9$) it takes around 70 min. On the other hand, for calcination at 857°C under 50% CO_2 ($P/P_{eq} = 0.9$) the reaction is started almost immediately after reaching the target temperature. At lower temperatures, calcination has already started when the 1st XRD scan is registered. Once CaO peaks emerge, $CaCO_3$ conversion (α, defined as the ratio of mass $CaCO_3$ calcined to its initial mass) can be obtained from a semi-quantitative (S-Q) analysis of the XRD scans as $(1-\alpha)/\alpha = \kappa\,(M_{CaCO3}/M_{CaO})(I_{104}/I_{200})$, where $\kappa \simeq 1.39$ is the ratio of calcite

to lime corundum numbers, $M_{CaCO3}/M_{CaO} = 100/56$ is the ratio of molecular weights and I_{104}/I_{200} is the ratio of calcite and lime main reflection peaks intensities. Figure 3 shows the time evolution of I_{104}/I_{200}, which is seen to decay exponentially with time as calcination progresses ($I_{104}/I_{200} \propto \exp(-\beta t)$). Thus, we may write

$$\alpha = \frac{1}{1 + \exp(-\beta(t - t_{1/2}))} \tag{8}$$

$$\frac{d\alpha}{dt} = \beta\alpha(1 - \alpha) \tag{9}$$

where $t_{1/2}$ is the time for half conversion. The time evolution of $CaCO_3$ conversion obtained for calcination tests at diverse conditions are plotted in Fig. 4. As may be seen, Eq. 8 provides a rather good fit to the data. From Eq. 9, $\beta = r(T, P)$ can be identified as the reaction rate (Eq. 3) whereas the mechanistic-rate function $f(\alpha) = \alpha(1 - \alpha)$ would conform to the Prout-Tompkins model [9, 32], which reflects the common observation of an induction period for heterogeneous reactions before initiation at nucleation sites where reactivity is locally enhanced due, for example, to the presence of structural defects. Accordingly, our experimental results show the existence of an induction period, which becomes extraordinarily prolonged at high temperatures and under CO_2 partial pressures close to the equilibrium pressure after which calcination proceeds extremely slow as seen above. As a general observation, we see that the longer the induction period is the slower calcination occurs afterwards.

Figure 5 shows data on the calcination reaction rate $r(T, P) = \beta$ inferred from the in-situ XRD analysis as a function of temperature and for the diverse values tested of the ratio P/P_{eq}. As predicted by the reaction rate model proposed elsewhere [18], we observe a change of behavior with temperature as depending on P/P_{eq}. For $P/P_{eq} \leqslant 0.7$ and

relatively low temperatures, the reaction rate increases with temperature according to an Arrhenius law (Eq. 4) with a positive activation energy of the order of the reaction enthalpy change. In contrast, for $P/P_{eq} \geqslant 0.8$ and high temperatures, the reaction rate is markedly decreased with temperature and turns to be characterized by a negative activation energy. Interestingly, the transition to negative activation energies is seen to occur at a critical value T_c that decreases with P/P_{eq}, which is in qualitative agreement with the theoretical expectation. Thus, it is $T_c \simeq 870$°C for $P/P_{eq} = 0.8$ whereas for $P/P_{eq} = 0.9$ it is $T_c \simeq 830$°C . The trends shown by the data agree with results obtained by means of thermogravimetric analysis (TGA) reported elsewhere [18].

B. The growth of CaO crystallite size

Figure 6 shows data on the nascent CaO crystallite size (L) as a function of $CaCO_3$ conversion (α), which have been calculated by means the Le Bail method [33] using the software TOPAS 4.2 (Bruker) [34]. The data demonstrates a clear correlation of crystallite size growth with the reaction rate. At the highest ratio of CO_2 partial pressure to equilibrium pressure ($P/P_{eq} = 0.9$), all the data conform to a logarithmic law ($L(\text{nm}) \simeq 110 + 25 \ln \alpha$) at calcination temperatures over $T \simeq 870$°C involving a very slow reaction kinetics. For temperatures above 890°C (CO_2 vol%>80%) the data suggest that L would reach a value close to $L_0 \simeq 110$ nm for $\alpha = 1$ (Fig. 6a). If $P/P_{eq} = 0.9$ is kept fixed and the calcination temperature is decreased, which speeds up calcination (as seen in the previous section), the growth of CaO crystallites deviates from the logarithmic law trend at an advanced state of conversion. Thus, for $T = 869$°C (60%CO_2), CaO crystallite size reaches a value of $L_0 \simeq 70$ nm for $\alpha \simeq 0.4$, which increases only slightly with conversion afterwards (Fig. 6a). Once conversion is ended ($\alpha = 1$), the size of crystallites continues to grow with time. As the

temperature is further decreased or P/P_{eq} is lowered down (the reaction becomes quicker) the value of L_0 is further decreased. For the fastest calcinations, the logarithmic trend is not observed since the first XRD pattern registered corresponds already to an advanced state of conversion giving a value of the crystallite size $L \simeq L_0$ which depends only weakly on conversion.

Figure 7 shows the time evolution of CaO crystallite size L and conversion α for two representative cases of slow and fast reaction kinetics. As can be seen, L increases with time at a low rate when the reaction is fast and conversion is finished ($\alpha = 1$) or near to completion. On the other hand, L is increased with time at a much larger rate when the reaction is slow (896°C , 90%CO_2) and conversion is not high yet ($\alpha < 0.5$). After this period (corresponding to the logarithmic dependence of L on α), L reaches a value $L = L_0$ that grows with time at a slow rate, which is similar to the rate of increase observed for quick calcination (730°C , 5%CO_2). The main difference in the crystallite size evolution between fast and slow calcination kinetics is thus the enhanced growth stage that takes place in the beginning of CaO nucleation at high CO_2 partial pressure at high temperature. The inferred values of L_0 from the data are plotted in Fig. 8a as a function of $1/T$ for the different values of P/P_{eq} tested. The data shows that L_0 is greatly increased with temperature nearby equilibrium ($P/P_{eq} \geq 0.8$). L_0 data is plotted in Fig. 8b as a function of the reaction rate r (1/min). As can be seen, L_0 is well correlated to the reaction rate by means of a power law $L_0(\text{nm}) \simeq 45 r^{-0.2}$.

Microscopic observations reported elsewhere on calcination of calcite crystal under vacuum suggest that the growth of CaO crystallites is due to the combination of oriented aggregation of metastable CaO^* nanocrystals due to surface attractive forces and sintering afterwards [3]. The time evolution of CaO crystallite size obtained in our work is consistent

with this view. Thus, CaO crystallites would evolve in two stages ruled by diverse physical mechanisms, namely aggregation and sintering afterwards. In a first stage, when conversion is still low, CaO* nanocrystals would aggregate into larger CaO crystals. The process of aggregation would be driven by the universal van der Waals interaction between solid surfaces resulting from the attractive forces between the fluctuating dipole moments of the molecules close to the surface. Aggregation would preponderate until conversion reaches a sufficiently high value and the presence of CaO* is reduced. Since the aggregation process would be characterized by a typical time scale, it would not lead to a significant enlargement of CaO crystallite size if calcination is very fast. On the other hand, aggregation would be enhanced for very slow calcination kinetics as suggested by the correlation between L_0 and the reaction rate (Fig. 8b). Moreover, it is well known that van der Waals attractive forces leading to aggregation are intensified by CO_2 adsorption on the surface of the interacting solids [35]. Since CO_2 adsorption is favored at conditions of high temperature and high P/P_{eq} [18] it is foreseeable that aggregation of CaO* nanocrystals would be promoted under these calcination conditions. Once conversion reaches an advanced state a major part of the crystallographic transformation would be completed and CaO stable crystallites mainly present would continue to grow by sintering. Our results indicate that, as compared to aggregation, sintering is less efficient in enlarging crystallite size. This is consistent with the fact that the calcination temperatures are well below the Tamman temperature $T_t \simeq 1170°C$ (the temperature for which diffusion of mobile species in a crystalline lattice leading to sintering becomes significant). Thus, most of crystallite growth would occur during the aggregation stage taking place at the initial stage of conversion.

It is well known that the CaO carbonation reactivity is directly related to crystallite size, the lower the size the highest the reactivity of CaO is [12, 17]. Thus, the CO_2 capture

efficiency in the CaL technology would be expectedly enhanced at calcination conditions that hinder CaO crystallite growth. According to our study, this goal would be achieved by hampering aggregation of the CaO* nanocrystals during the crystallographic transformation. Arguably, that is a main effect of the addition of inert nanocrystals into the structure of CaO based synthetic sorbents with enhanced multicyclic stability [36]. Natural dolomite ($CaMg(CO_3)_2$) is a clear example where this mechanism might play a role. Thus, inert MgO nanocrystals would hinder the aggregation of CaO nanocrystals during the crystallographic transformation. As seen in a recently reported study, the multicyclic reactivity of CaO derived from dolomite is greatly enhanced at CaL conditions (involving high CO_2 partial pressure in the calcination environment) as compared to CaO derived from limestone [37, 38]. Usually, the effect of MgO or inert nano-additives employed in synthetic sorbents [36] is attributed to their higher Tamman temperature as compared to CaO. Yet, the Tamman temperature for MgO ($T_t \simeq 1276$°C) is just slightly above the CaO Tamman temperature [39]. The main difference between MgO and CaO in the CaL process is that the latter suffers in each cycle a crystallographic transformation whereas the former is inert and remains stable along the cycles. CaO crystallite growth in short calcination times would be thus mainly driven by aggregation during the $CaCO_3$/CaO crystallographic transformation and not to sintering after calcination is complete. In agreement with this argument, it is observed that the multicyclic carbonation of dolomite is not improved as compared to limestone when calcination is carried out under air at reduced temperatures [37]. According to our study, aggregation and sintering of the nascent CaO crystals would not be as relevant at these mild calcination conditions as for calcination under high CO_2 partial pressure [40]. Thus, the activities of CaO derived from limestone and dolomite decay with the calcination/carbonation cycle number at a similar and relatively small rate [37].

C. The $CaCO_3$/CaO crystallographic transformation

In-situ observations of calcite crystals calcination in vacuo by means of transmission electron microscopy coupled with selected area electron diffraction (TEM-SAED) and 2D-XRD analysis [3] have recently evidenced that calcination of $CaCO_3$ occurs through a solid state topotactic reaction as was firstly hypothesized by Hyatt et al. in 1958 [41]. Accordingly, a metastable structure consisting of rod-shaped CaO^* nanocrystals is firstly developed on each rhombohedral cleavage face of the calcite pseudomorph [3]. Earlier studies had already shown evidences that limestone calcination should involve a crystallographic transformation [11–16]. Nevertheless, experimental measurements based on ex-situ XRD conventional analysis could not yield a clear description on the orientation relationships of the metastable CaO^* phase. It must be noticed that calcination tests in these works were all made at high temperatures either under vacuum or very low CO_2 partial pressure (usually air or inert gases). Under these conditions, the structural transformation is extremely fast. On the other hand, the very slow calcination observed in our in-situ XRD tests at high temperatures and nearby equilibrium might allow us to identify the footprint and role of the metastable CaO^* phase on the reaction progress by means of a quantitative analysis of the in-situ XRD scans registered during the transformation.

In order to quantify the presence of an intermediate CaO^* metastable structure, an accurate quantitative phase Rietveld analysis of the XR scans must be performed. To this end, XRD patterns were recorded during in-situ calcination tests in a wide range of diffraction angles ($18° < 2\theta < 118°$). Even though recording each diffractogram in this wide range of angles takes about 7.5 min, which would preclude in principle an accurate time resolution to investigate the calcination kinetics, these wide scans serve us to register the intensity of

a large number of reflection peaks, which improves the robustness of the Rietveld analysis results. Moreover, we will restrict our study to calcination conditions yielding a very slow kinetics ($P/P_{eq} = 0.9$, $T \geq 869$°C), which expectedly lead to a noticeable presence of CaO* . It must be also remarked that the experimental equipment used allows registering a rather large number of counts for each one of the diffraction peaks as required to carry out a robust quantitative analysis.

According to the crystallographic transformation details that have been inferred from in-situ calcination observations under vacuum we will assume that the CaO* metastable phase stems as a pseudomorph formed from calcite ($CaCO_3$) before the nucleation of lime (CaO) [3]. Figure 9 shows the crystallographic unit cells of the three phases ($CaCO_3$ calcite, CaO* , and CaO lime) that would be expectedly involved in the calcination reaction [3]. The hexagonal rhombohedral calcite structure (space group R-3c, 167) yields at the reaction temperature the cubic metastable CaO* structure (space group Fm-3m, 225) as a dilated pseudomorph of lime (same space group that CaO*) which appears afterwards. The cell parameters for a temperature of 900°C are for calcite b=4.97 Å and c=17.64 Å, for CaO* it is a* =5.31 Å and a=4.86 Å for lime. Figure 10 schematizes the evolution from calcite to CaO* . In a) the unit cell of calcite ($CaCO_3$) is depicted with all the atoms. In b) the cell is shown with only the C and O atoms. Ca atoms have been hidden for the sake of clarity to illustrate the transformation. C and O atoms form CO_3^{2-} ions placed in the same plane. CO_2 is released upon chemical decomposition and escapes from the cell. In d) and e) the $(10\underline{1}4)$ calcite plane is displayed where the Ca^{2+} and CO_3^{2-} ions can be seen and the marked CO_2 molecules before being released. In e) the arrows indicate the displacement of the Ca and O atoms remaining in the structure after CO_2 is released, which leads to the metastable CaO* structure. Figure 10e) shows the $(1\underline{1}0)$ plane of the resulting cubic CaO* structure.

The quantitative phase analysis on the registered XRD scans has been carried out by means of Rietveld method [42] using the software TOPAS 4.2 (Bruker) [34]. Zero error (2θ), sample displacement, absorption (1/cm) and lattice parameters of the phases were allowed to vary to provide the best fits. Importantly, dilation of the structures as affected by temperature is considered in the analysis. The background was fitted by a fifth-order Chebychev polynomial. Lorentz and polarization geometric factors for the measurement configuration were used. For the fittings to be as accurate as possible the GOF (Goodness-of-fit) should be greater than 1, and as close as possible to it [42]. Furthermore, the residual factors (Rwp and RBrag) have to be small for the measurement configuration used [42]. In general, acceptable fitting indicators were obtained in our analysis (GOF$\sim$1-1.5, Rwp$\sim$10, RBragg$\sim$1). The difficulty of early works to identify a metastable phase [16] from ex-situ 2D-XRD analysis can be explained on the basis that the CaO* structure yields a main reflection peak (111) at an angle close to the main peak (104) position of the $CaCO_3$ structure. Moreover, calcination tests have been mostly carried under vacuum or air. In these conditions, the structural transformation is extremely fast and the metastable CaO* phase disappears quickly. In our work, the high level of in-situ XRD technical accuracy achieved as well as the slow reaction kinetics at conditions close to equilibrium and high temperatures enable us to infer the presence of CaO* during the crystallographic transformation according to the crystallographic structure suggested elsewhere [3]. Figure 11 shows an example of the Rietveld analysis results on a XRD pattern, which yields the weight % of the three phases involved in the transformation. A zoom of the angle intervals comprising the CaO* reflection peaks can be seen in Fig. 12. As may be observed, the asymmetry of the main experimental peak (Fig. 12a) is accounted for by the contribution of the (111) CaO* peak to obtain a good fit. On the other hand, the experimental reflected intensity between $2\theta \simeq 57.4^\circ$ and

362 58° needs from the contribution of the (311) CaO* peak to get a satisfactory fit.

363 Figure 13a-c shows time evolution data on the wt% measured for the three phases in-
364 volved in the crystallographic transformation. At $P/P_{eq} = 0.9$ and high temperatures the
365 transformation CaO* →CaO is nearly frozen, which allows detecting a remarkable presence
366 of CaO* around 10% even before the stable CaO crystals nucleate. Thus, chemical decom-
367 position would have occurred during the long induction period preceding the nucleation of
368 CaO, which is hampered by the unfavorable conditions (high temperatures and CO_2 partial
369 pressure near to equilibrium) for the exothermic transformation CaO* →CaO to take place.
370 At these conditions, $CaCO_3$ conversion reaches a small value at the end of the calcination
371 tests at $T = 903$°C and 895°C ($\alpha < 0.15$) and CaO* wt% is kept at a high value even after
372 nucleation of the CaO phase. This observation would uphold the argument on aggregation of
373 CaO* nanocrystals as a driving mechanism for CaO crystal growth, which would be relevant
374 during slow calcination as long as the presence of CaO* is kept at a high level. Fig. 13d
375 shows data on the calculated CaO* wt% as a function of conversion. Interestingly, the data
376 adjusts to a common trend independently of the calcination temperature and CO_2 vol%. As
377 long as conversion is small, the wt% of CaO* remains around 10% whereas it drops to zero
378 when $CaCO_3$ conversion is above $\alpha \simeq 0.5$, which is reached in the test carried out at 869°C
379 (60% CO_2). In agreement with the role of CaO* nanocrystals aggregation on CaO crystal
380 growth, the disappearance of the CaO* phase is seen to coincide with the end of enhanced
381 growth of the CaO crystallite size.

382 $CaCO_3$ conversion data as a function of time directly derived from the Rietveld quanti-
383 tative analysis are plotted in Fig. 14. The figure shows also conversion data derived from
384 a semi-quantitative analysis (SQ) of the short-time scans (140 s long) registered within a
385 reduced window of diffraction angles (Fig. 3a) and using the ratio of intensities of main

$CaCO_3$ and CaO peaks. As can be seen, both analysis yield a similar conversion data, which supports the validity of the kinetics study described above based on a SQ analysis.

IV. CONCLUSIONS

Calcination of limestone under CO_2 becomes extraordinarily slow as the temperature is increased at CO_2 partial pressures nearby the equilibrium pressure ($P/P_{eq} \lesssim 1$). According to the mechanism proposed elsewhere, the reaction is initiated by the endothermic decomposition of $CaCO_3$ after which CO_2 is desorbed while a metastable CaO^* form transforms into the stable CaO phase. If the partial pressure of CO_2 in the calcination environment is very small as compared to the equilibrium pressure ($P/P_{eq} \ll 1$), structural transformation and desorption occur extremely fast and calcination is just rate-limited by chemical decomposition. On the other hand, CO_2 desorption is hindered at CO_2 partial pressures near to the equilibrium pressure whereas the activity of the metastable CaO^* form decreases as the temperature is increased. As a result, calcination is significantly hampered by an increase of temperature if P/P_{eq} is kept fixed and close to unity. In the present manuscript, the crystallographic $CaCO_3$/CaO transformation at these conditions has been studied in detail by means of in-situ XRD analysis. A main conclusion is that calcination kinetics, the presence of an intermediate CaO^* metastable form and the growth of CaO crystallite are closely related. Nearby equilibrium ($P/P_{eq} \lesssim 1$), calcination at high temperatures is characterized by a long induction period after which CaO nucleates at a very slow rate. A steady wt% of CaO^* is detected by a significant amount during the induction period and CaO nucleation. Results on CaO crystallite size suggest that CaO crystallites grow during nucleation at a high rate as driven by aggregation of CaO^* nanocrystals. As conversion reaches an advanced state ($\alpha \gtrsim 0.5$), the wt% of the CaO^* phase drops to zero whereas, at the same time, the

growth of CaO crystallites proceeds at a much slower rate as just driven by sintering. Since the calcination temperatures applied are well below the Tamman temperature, aggregation plays a preponderant role on the final size of the CaO crystallites, which is thus correlated to the reaction rate. Calcination conditions yielding slow kinetics (high P/P_{eq} and high temperature) favor aggregation of the CaO* nanocrystals during a prolonged period, which leads to a large size of the CaO crystallites. On the other hand, if calcination is fast the metastable CaO* phase is present just for very short times, which limits the growth of CaO crystallites. The fundamental understanding gained in this work on the calcination reaction might be used for practical applications in which the control of the reaction kinetics and CaO crystallite size is relevant. For example, the Ca-Looping technology for CO_2 capture relies on the fast carbonation of CaO derived from limestone calcination under high CO_2 partial pressure. Since CaO carbonation reactivity is inversely correlated to the size of CaO crystallites, CO_2 capture would be enhanced by reducing the strength of surface attractive forces that drive aggregation of CaO* nanocrystals during the crystallographic $CaCO_3$/CaO transformation, which would be achieved by the insertion of inert nanocrystals in synthetic sorbents or the presence of inert MgO nanocrystals in dolomite. Thus, our work provides a possible explanation on the enhanced CaO capture capacity displayed by these materials as compared to limestone at CaL conditions.

V. ACKNOWLEDGEMENTS

This work was supported by the Andalusian Regional Government Junta de Andalucia (contract FQM-5735), Spanish Government Agency Ministerio de Economia y Competitividad (contract CTQ2014-52763-C2-2-R). We gratefully acknowledge the X-ray service of the Innovation, Technology and Research Center of the University of Seville (CITIUS).

VI. REFERENCES

[1] R. S. Boynton, *Chemistry and Technology of Lime and Limestone*. New York: Wiley, 1980. For general practical information, the interested reader is recommended perusal of the first edition (1966).

[2] B. V. L'vov, L. K. Polzik, and V. L. Ugolkov, "Decomposition kinetics of calcite: a new approach to the old problem," *Thermochimica Acta*, vol. 390, no. 1 -2, pp. 5 – 19, 2002.

[3] C. Rrodriguez-Navarro, E. Ruiz-Agudo, A. Luque, A. B. Navarro, and M. Ortega-Huertas, "Thermal decomposition of calcite: Mechanisms of formation and textural evolution of cao nanocrystals," *American Mineralogist*, vol. 94, p. 578 593, 2009.

[4] P. Michele, F. Loic, and S. Michel, "From the drawbacks of the Arrhenius-f(α) rate equation towards a more general formalism and new models for the kinetic analysis of solid - gas reactions," *Thermochimica Acta*, vol. 525, no. 1–2, pp. 93 – 102, 2011.

[5] I. Barin, *Thermochemicaldata of pure substances*. Weinheim: VCH., 1989.

[6] F. Garcia-Labiano, A. Abad, L. de Diego, P. Gayan, and J. Adanez, "Calcination of calcium-based sorbents at pressure in a broad range of CO_2 concentrations," *Chemical Engineering Science*, vol. 57, no. 13, pp. 2381 – 2393, 2002.

[7] B. Stanmore and P. Gilot, "Review - calcination and carbonation of limestone during thermal cycling for CO_2 sequestration," *Fuel Processing Technology*, vol. 86, no. 16, pp. 1707 – 1743, 2005.

[8] J. M. Criado, M. Gonzalez, J. Malek, and A. Ortega, "The effect of the CO_2 pressure on the thermal decomposition kinetics of calcium carbonate," *Thermochimica Acta*, vol. 254, pp. 121

– 127, 1995.

[9] A. Khawam and D. R. Flanagan, "Solid-state kinetic models: Basics and mathematical fundamentals," *The Journal of Physical Chemistry B*, vol. 110, no. 35, pp. 17315 – 17328, 2006.

[10] A. K. Galwey and M. E. Brown, "Application of the Arrhenius equation to solid state kinetics: can this be justified?," *Thermochimica Acta*, vol. 386, no. 1, pp. 91 – 98, 2002.

[11] D. Beruto and A. W. Searcy, "Use of the langmuir method for kinetic studies of decomposition reactions: calcite ($CaCO_3$)," *J. Chem. Soc., Faraday Trans. 1*, vol. 70, pp. 2145–2153, 1974.

[12] D. Beruto, A. W. Searcy, and M. G. Kim, "Calcium oxides of high reactivity," *Nature*, vol. 5574, pp. 221 – 222, 1976.

[13] A. W. Searcy and D. Beruto, "Kinetics of endothermic decomposition reactions. i. steady-state chemical steps," *The Journal of Physical Chemistry*, vol. 80, no. 4, pp. 425–429, 1976.

[14] K. M. Towe, "Ultrastructure of calcite decomposition in vacuo," *Nature*, vol. 274, pp. 239 – 240, 1978.

[15] S. Dash, M. Kamruddin, P. Ajikumar, A. Tyagi, and B. Raj, "Nanocrystalline and metastable phase formation in vacuum thermal decomposition of calcium carbonate," *Thermochimica Acta*, vol. 363, no. 1-2, pp. 129–135, 2000.

[16] D. Beruto, A. W. Searcy, and M. G. Kim, "Microstructure, kinetic, structure, thermodynamic analysis for calcite decomposition: free-surface and powder bed experiments," *Thermochimica Acta*, vol. 424, no. 1 2, pp. 99 – 109, 2004.

[17] J. M. Valverde, P. E. Sanchez-Jimenez, and L. A. Perez-Maqueda, "Limestone calcination nearby equilibrium: Kinetics, cao crystal structure, sintering and reactivity," *The Journal of Physical Chemistry C*, vol. 119, no. 4, pp. 1623–1641, 2015.

[18] J. M. Valverde, "On the negative activation energy for limestone calcination at high temperatures nearby equilibrium," *Chemical Engineering Science*, vol. 132, pp. 169–177, 2015.

[19] J. Blamey, E. J. Anthony, J. Wang, and P. S. Fennell, "The calcium looping cycle for large-scale CO_2 capture," *Prog. Energ. Combust. Sci.*, vol. 36, no. 2, pp. 260–279, 2010.

[20] M. C. Romano, "Modeling the carbonator of a Ca-looping process for CO_2 capture from power plant flue gas," *Chemical Engineering Science*, vol. 69, pp. 257 – 269, 2012.

[21] B. Arias, M. Diego, J. Abanades, M. Lorenzo, L. Diaz, D. Martinez, J. Alvarez, and A. Sanchez-Biezma, "Demonstration of steady state CO_2 capture in a 1.7 MWth calcium looping pilot," *International Journal of Greenhouse Gas Control*, vol. 18, pp. 237–245, 2013.

[22] J. Ströhle, M. Junk, J. Kremer, A. Galloy, and B. Epple, "Carbonate looping experiments in a 1MWth pilot plant and model validation," *Fuel*, vol. 127, no. 0, pp. 13 – 22, 2014. Fluidized Bed Combustion and Gasification CO2 and SO2 capture: Special Issue in Honor of Professor E.J. (Ben) Anthony.

[23] A. Charitos, N. Rodriguez, C. Hawthorne, M. Alonso, M. Zieba, B. Arias, G. Kopanakis, G. Scheffknecht, and J. C. Abanades, "Experimental validation of the Calcium Looping CO_2 capture process with two circulating fluidized bed carbonator reactors," *Industrial & Engineering Chemistry Research*, vol. 50, no. 16, pp. 9685–9695, 2011.

[24] A. Martinez, Y. Lara, P. Lisbona, and L. M. Romeo, "Energy penalty reduction in the calcium looping cycle," *International Journal of Greenhouse Gas Control*, vol. 7, pp. 74 – 81, 2012.

[25] I. Martinez, G. Grasa, R. Murillo, B. Arias, and J. Abanades, "Modelling the continuous calcination of $CaCO_3$ in a Ca-looping system," *Chemical Engineering Journal*, vol. 215–216, pp. 174–181, 2013.

[26] R. T. Symonds, D. Y. Lu, V. Manovic, and E. J. Anthony, "Pilot-scale study of CO_2 capture by cao-based sorbents in the presence of steam and SO_2," *Industrial & Engineering Chemistry Research*, vol. 51, no. 21, pp. 7177 – 7184, 2012.

[27] A. Coppola, F. Scala, P. Salatino, and F. Montagnaro, "Fluidized bed calcium looping cycles for CO_2 capture under oxy-firing calcination conditions: Part 1. assessment of six limestones," *Chemical Engineering Journal*, vol. 231, pp. 537 – 543, 2013.

[28] N. Rodriguez, M. Alonso, G. Grasa, and J. C. Abanades, "Heat requirements in a calciner of $CaCO_3$ integrated in a CO_2 capture system using CaO," *Chemical Engineering Journal*, vol. 138, no. 1–3, pp. 148–154, 2008.

[29] L. M. Romeo, Y. Lara, P. Lisbona, and J. M. Escosa, "Optimizing make-up flow in a CO_2 capture system using CaO," *Chemical Engineering Journal*, vol. 147, no. 2-3, pp. 252 – 258, 2009.

[30] A. Martinez, Y. Lara, P. Lisbona, and L. M. Romeo, "Operation of a cyclonic preheater in the Ca-looping for CO_2 capture," *Environmental Science & Technology*, vol. 47, no. 19, pp. 11335–11341, 2013.

[31] G. Grasa, R. Murillo, M. Alonso, and J. C. Abanades, "Application of the random pore model to the carbonation cyclic reaction," *AIChE J.*, vol. 55, no. 5, pp. 1246–1255, 2009.

[32] M. E. Brown, "The prout-tompkins rate equation in solid-state kinetics," *Thermochimica Acta*, vol. 300, no. 1 - 2, pp. 93 – 106, 1997.

[33] A. Le Bail, "Whole powder pattern decomposition methods and applications: A retrospection," *Powder Diffraction*, vol. 20, pp. 316–326, 12 2005.

[34] A. Bruker, "Topas 4.2 user manual," *Bruker AXS GmbH, Karlsruhe, Germany Search PubMed*, 2009.

[35] H.-Y. Xie and D. Geldart, "Fluidization of FCC powders in the bubble-free regime: effect types of gases and temperature," *Powder Technol.*, vol. 82, pp. 269 – 277, 1995.

[36] J. M. Valverde, "Ca-based synthetic materials with enhanced CO_2 capture efficiency," *J. Mater. Chem. A.*, vol. 1, p. 447 468, 2013.

[37] J. Valverde, P. Sanchez-Jimenez, and L. Perez-Maqueda, "Ca-looping for postcombustion $\{CO_2\}$ capture: A comparative analysis on the performances of dolomite and limestone," *Applied Energy*, vol. 138, no. 0, pp. 202 – 215, 2015.

[38] A. Coppola, F. Scala, P. Salatino, and F. Montagnaro, "Fluidized bed calcium looping cycles for CO_2 capture under oxy-firing calcination conditions: Part 2. assessment of dolomite vs. limestone," *Chemical Engineering Journal*, vol. 231, pp. 544 – 549, 2013.

[39] A. M. Kierzkowska, R. Pacciani, and C. R. Müller, "CaO-based CO_2 sorbents: From fundamentals to the development of new, highly effective materials," *ChemSusChem*, vol. 6, no. 7, pp. 1130–1148, 2013.

[40] J. M. Valverde, P. E. Sanchez-Jimenez, and L. A. Perez-Maqueda, "Calcium-looping for post-combustion CO_2 capture. on the adverse effect of sorbent regeneration under CO_2," *Applied Energy*, vol. 126, pp. 161–171, 2014.

[41] E. P. Hyatt, I. B. Cutler, and M. E. Wadsworth, "Calcium carbonate decomposition in carbon dioxide atmosphere," *Journal of the American Ceramic Society*, vol. 41, no. 2, pp. 70–74, 1958.

[42] R.-A. Y. (Ed.), *The Rietveld Method*. No. 5 in IUCr Monographs on Crystallography, New York: Oxford University Press, 1993.

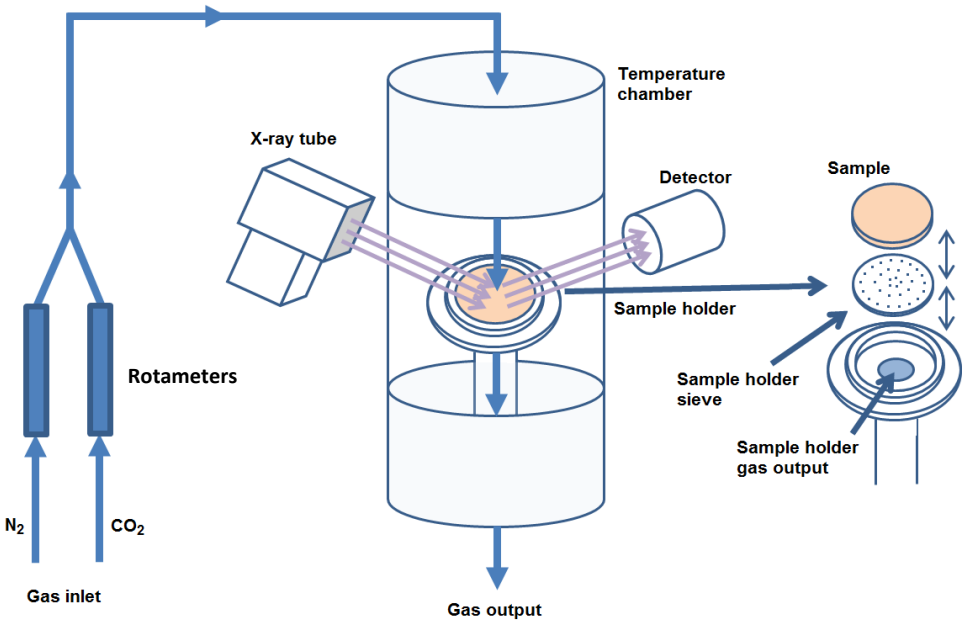

FIG. 1: Schematic layout of the experimental setup.

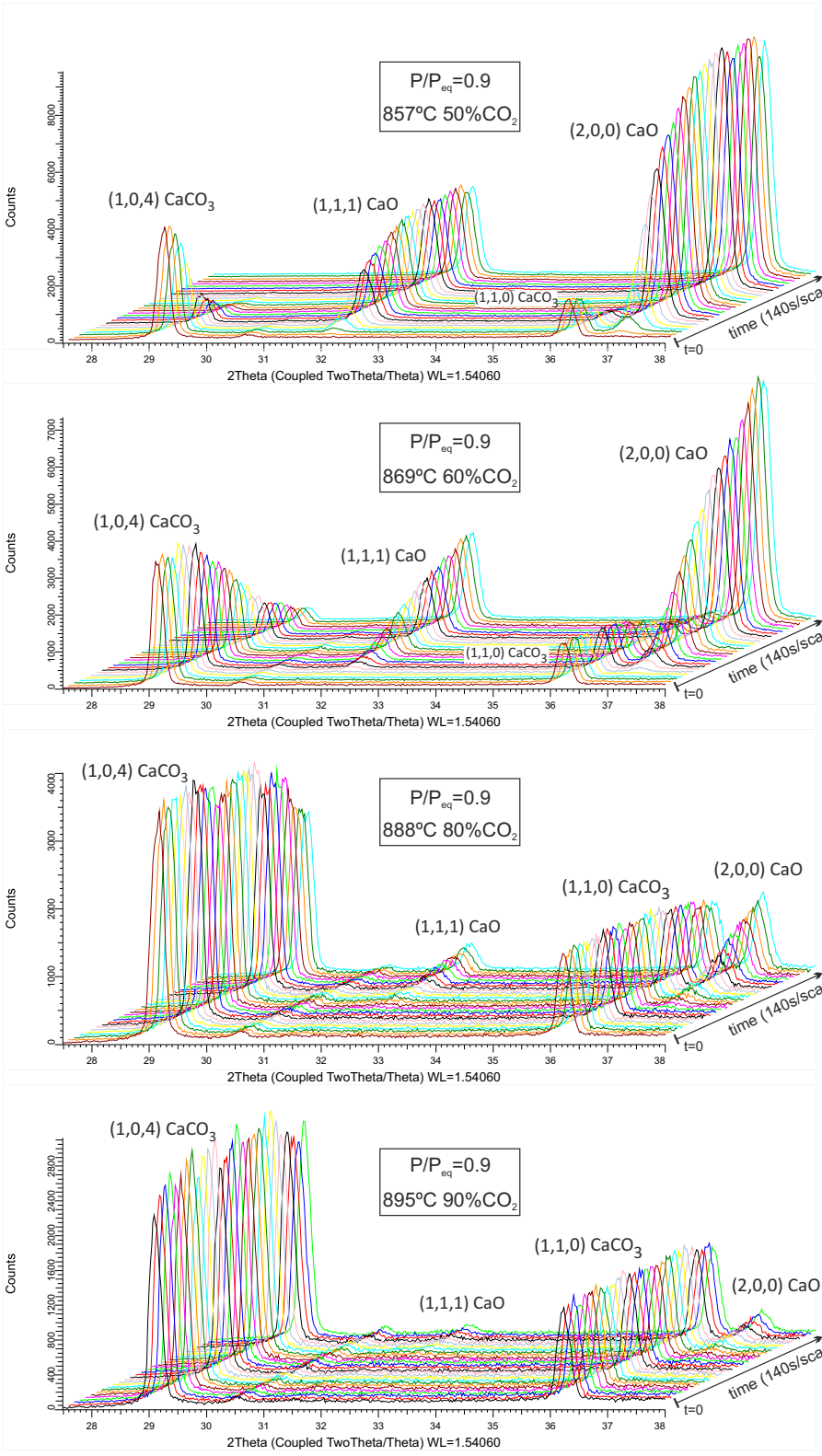

FIG. 2: Diffractograms recorded by in-situ XRD analysis during calcination of natural limestone at diverse temperatures and CO_2 vol% in the calcination environment yielding a ratio of the partial CO_2 pressure to equilibrium pressure $P/P_{eq} = 0.9$. Main Bragg peaks of calcite ($CaCO_3$: Rombo.H.axes, space group R-3C (163))) and lime (CaO: Cubic, space group Fm-3m (225)) are indicated.

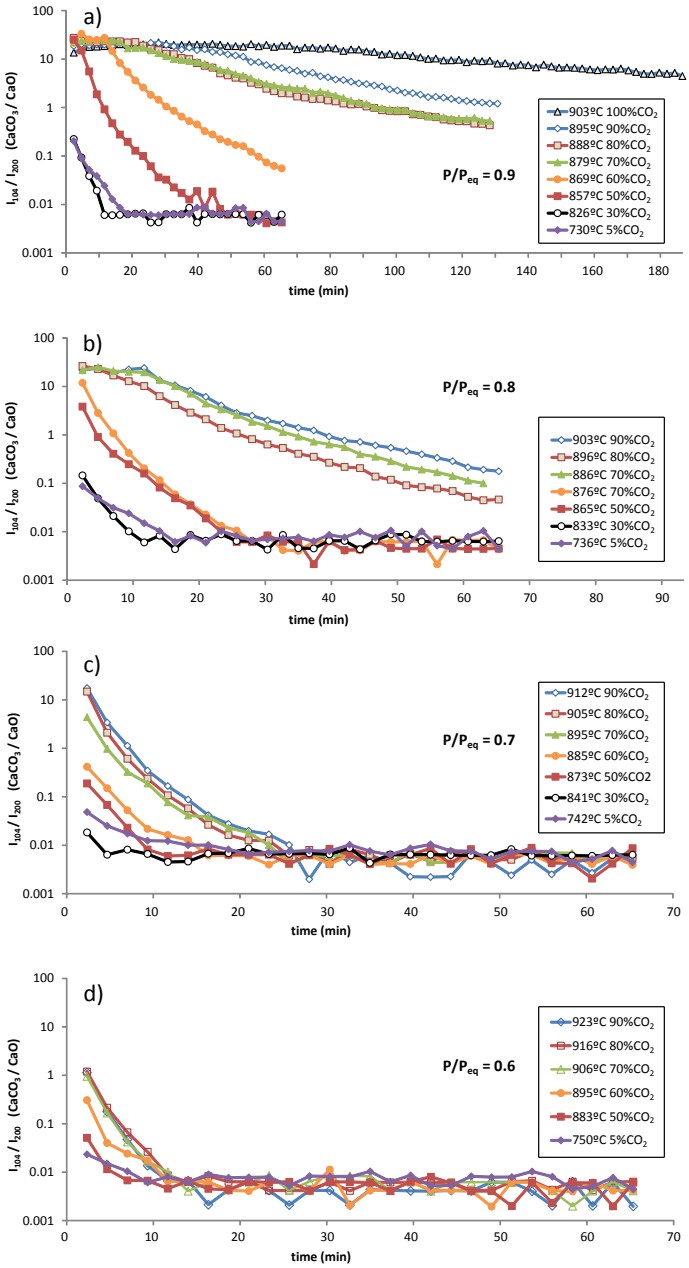

FIG. 3: Ratio of $CaCO_3$ (104) main reflection peak intensity to CaO (200) main reflection peak intensity during in-situ calcination tests at diverse temperatures and under different CO_2 vol%. Data series in each graph correspond to same values of the ratio of CO_2 partial pressure to equilibrium pressure (P/P_{eq}) as indicated. Note the vertical log scale and the diverse time scales.

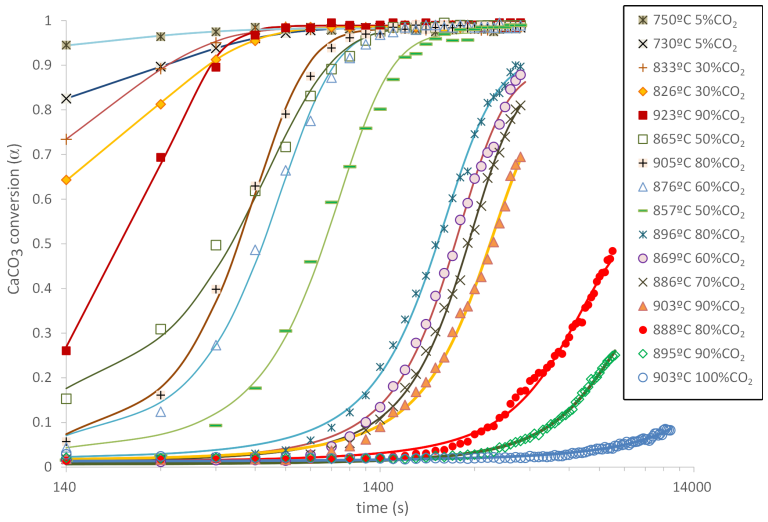

FIG. 4: Time evolution of $CaCO_3$ conversion obtained from in-situ XRD semi-quantitative analysis for calcination tests at the indicated conditions. The solid lines represent the best fits using a sigmoidal function (Eq. 8).

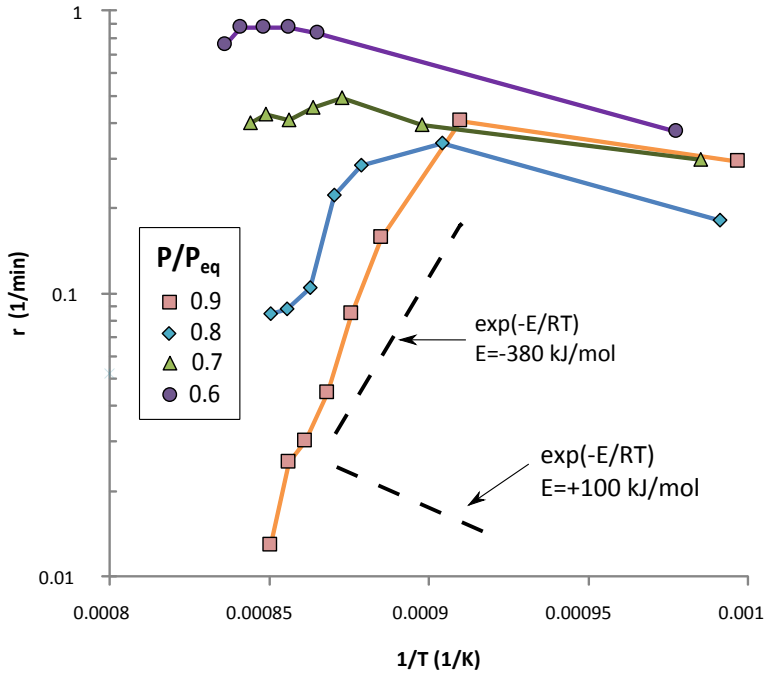

FIG. 5: Reaction rate r as a function of $1/T(K)$ for calcination tests as obtained from in-situ XRD semi-quantitative analysis. The dashed lines show the theoretically predicted trends $r \propto \exp(-E/RT)$ for the values indicated of the activation energy E.

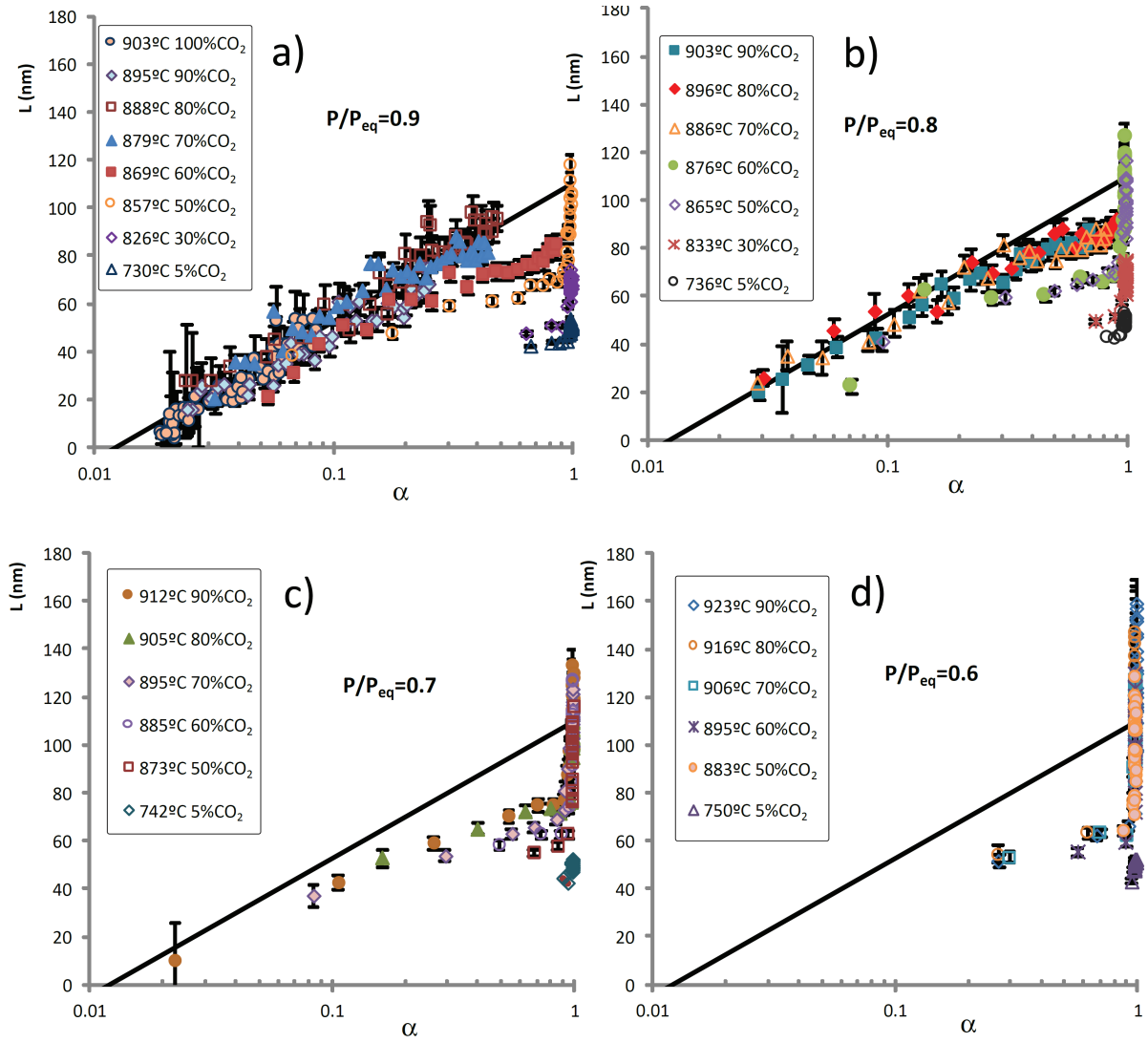

FIG. 6: CaO crystallite size (L) as a function of $CaCO_3$ conversion (α) calculated by Le Bail analysis of in-situ XRD diffractograms. Calcination tests in each graph were carried out at the indicated conditions and correspond to a given value of P/P_{eq}. The solid line represents the equation $L = 110 + 25 \ln \alpha$ nm.

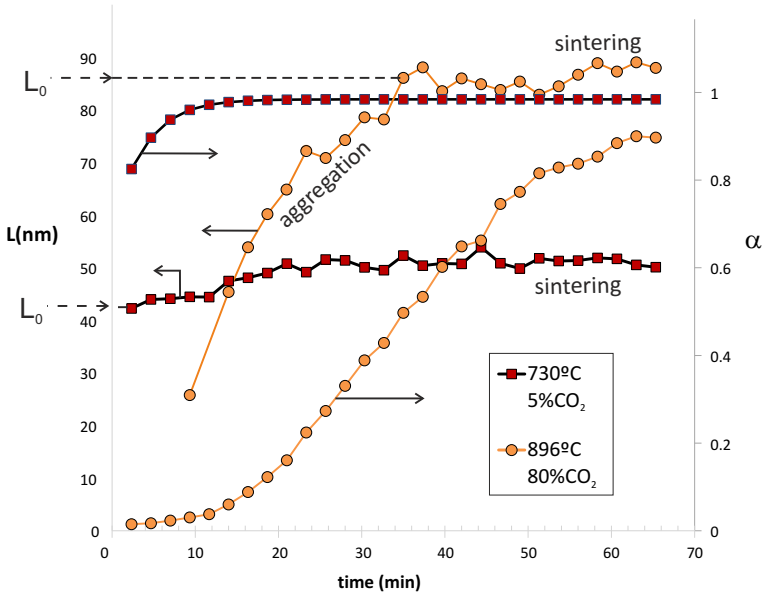

FIG. 7: Time evolution of CaO crystallite size (L) and $CaCO_3$ conversion (α) for calcination conditions yielding slow (896°C /80%CO_2) and fast (730°C /5%CO_2) calcination kinetics. The two stages (aggregation and sintering) inferred on the growth of CaO crystallite size are indicated.

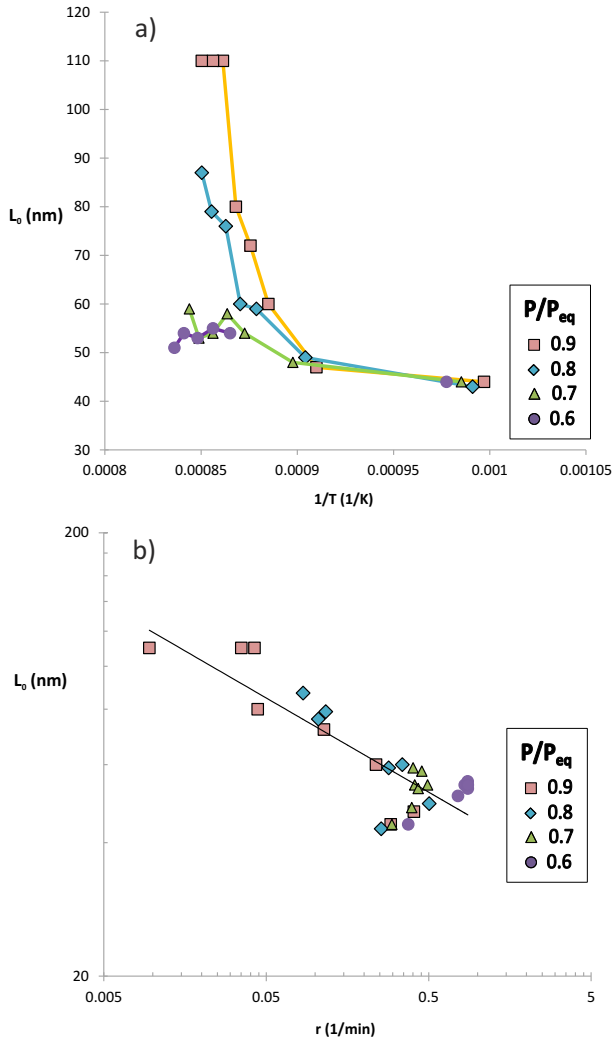

FIG. 8: a) CaO crystallite size (L_0) at the end of the aggregation stage as a function of $1/T$. b) Same data plotted versus the reaction rate r (1/min) measured (Fig. 5). The solid line is the best power law fit ($L_0 \simeq 45\, r^{-0.2}$)

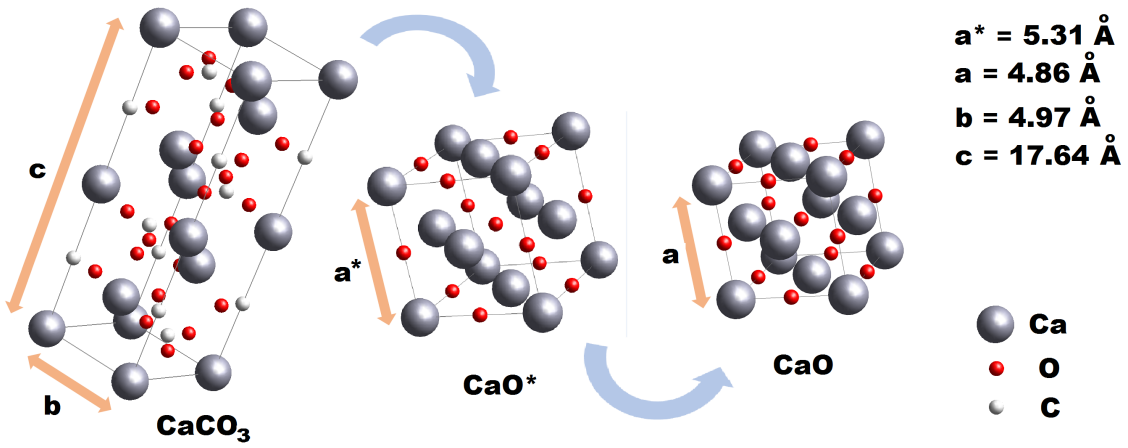

FIG. 9: Hexagonal rhombohedral calcite structure (space group R-3c, 167) yielding during calcination a cubic metastable CaO* structure (space group Fm-3m, 225) as a dilated pseudomorph of lime (same space group that CaO*) that appears afterwards. The cell parameters indicated correspond to a temperature of 900°C .

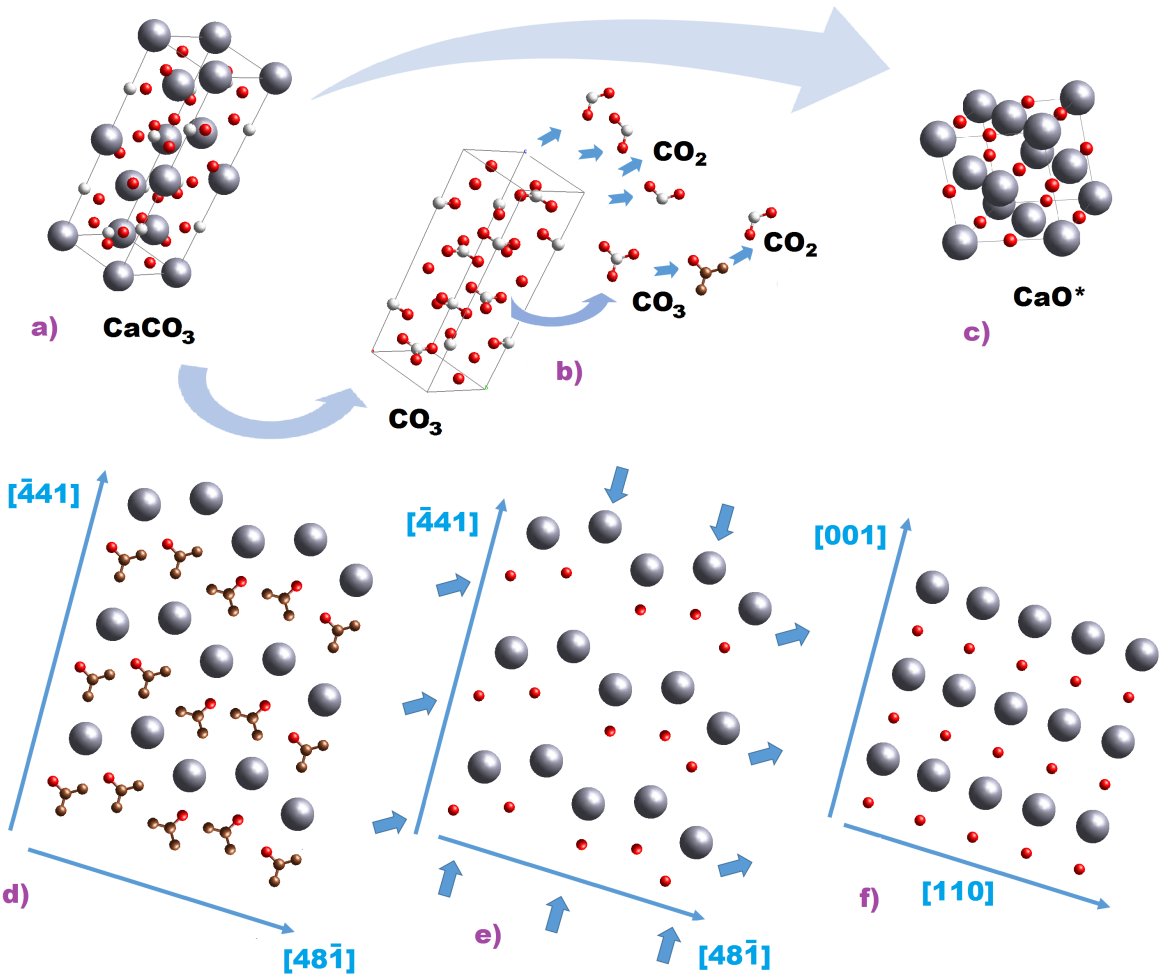

FIG. 10: Schematic representation of the crystallographic evolution of $CaCO_3$ to CaO^* . a) Calcite structure; b) shows the same structure with hidden Ca atoms and how the CO_2 is released; c) shows the CaO^* resulting structure; d) and e) show the $(10\underline{1}4)$ calcite plane. In d) the CO_2 molecule is colored. In e) CO_2 is released. The arrows mark the direction toward the remaining Ca and O atoms move; e) shows the cubic structure of the CaO^* in the $(1\underline{1}0)$ plane.

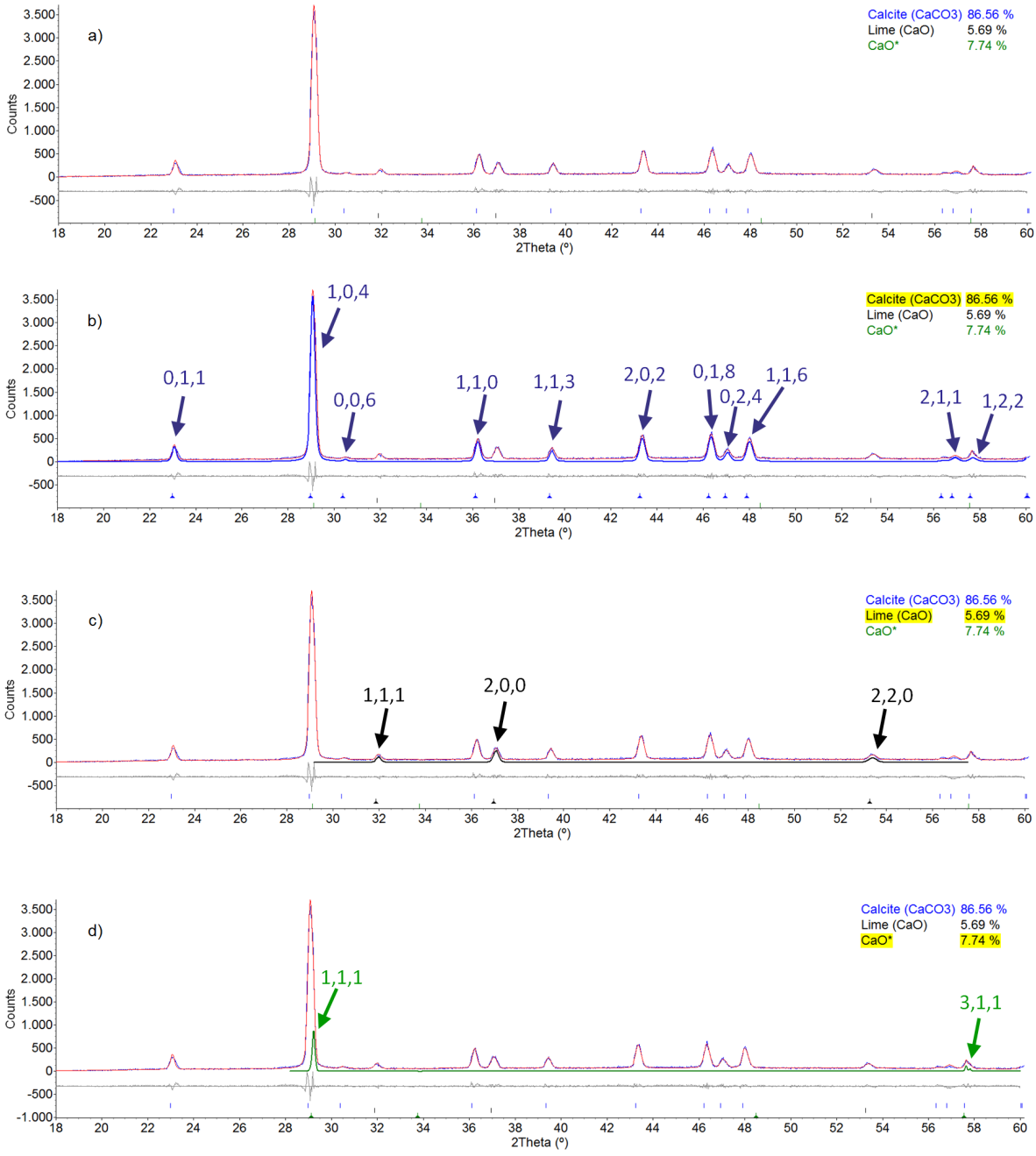

FIG. 11: a) Experimental diffractogram obtained during in-situ calcination at 903°C /100%CO_2 (t=210 min, blue line) and Rietveld best fit (red). The bottom grey line shows the deviation between the best fit and experimental diffractograms. Figures b) to d) show the XRD patterns obtained from the best fit for each one of the three phases present in the indicated wt% (b: calcite, c: lime, d: CaO*).

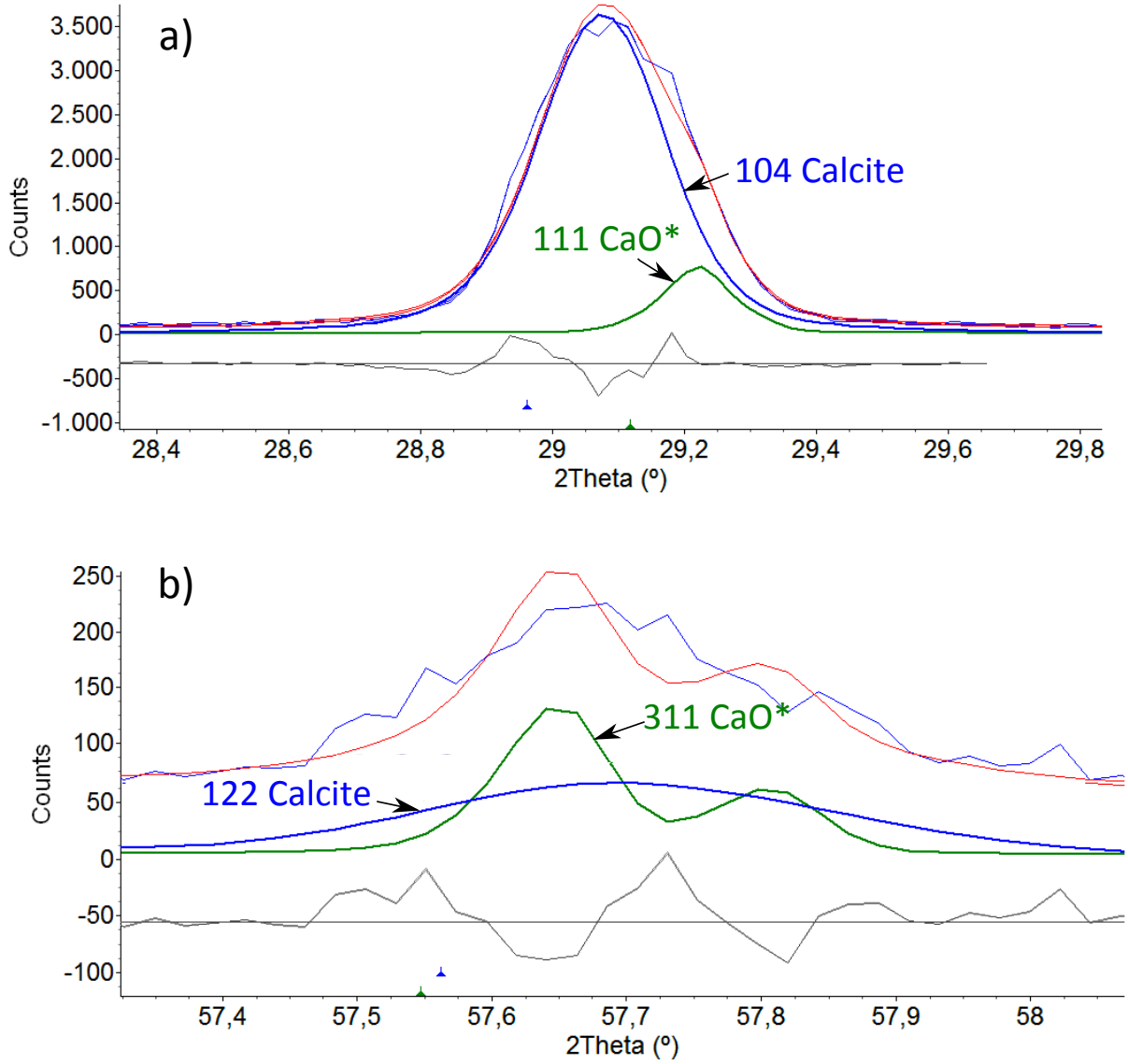

FIG. 12: Zooms of the diffractogram shown in Fig. 11 illustrating the contribution of the reflection peaks from the CaO* phase from the best Rietveld fit (red thin line) to the experimental pattern (blue thin line).

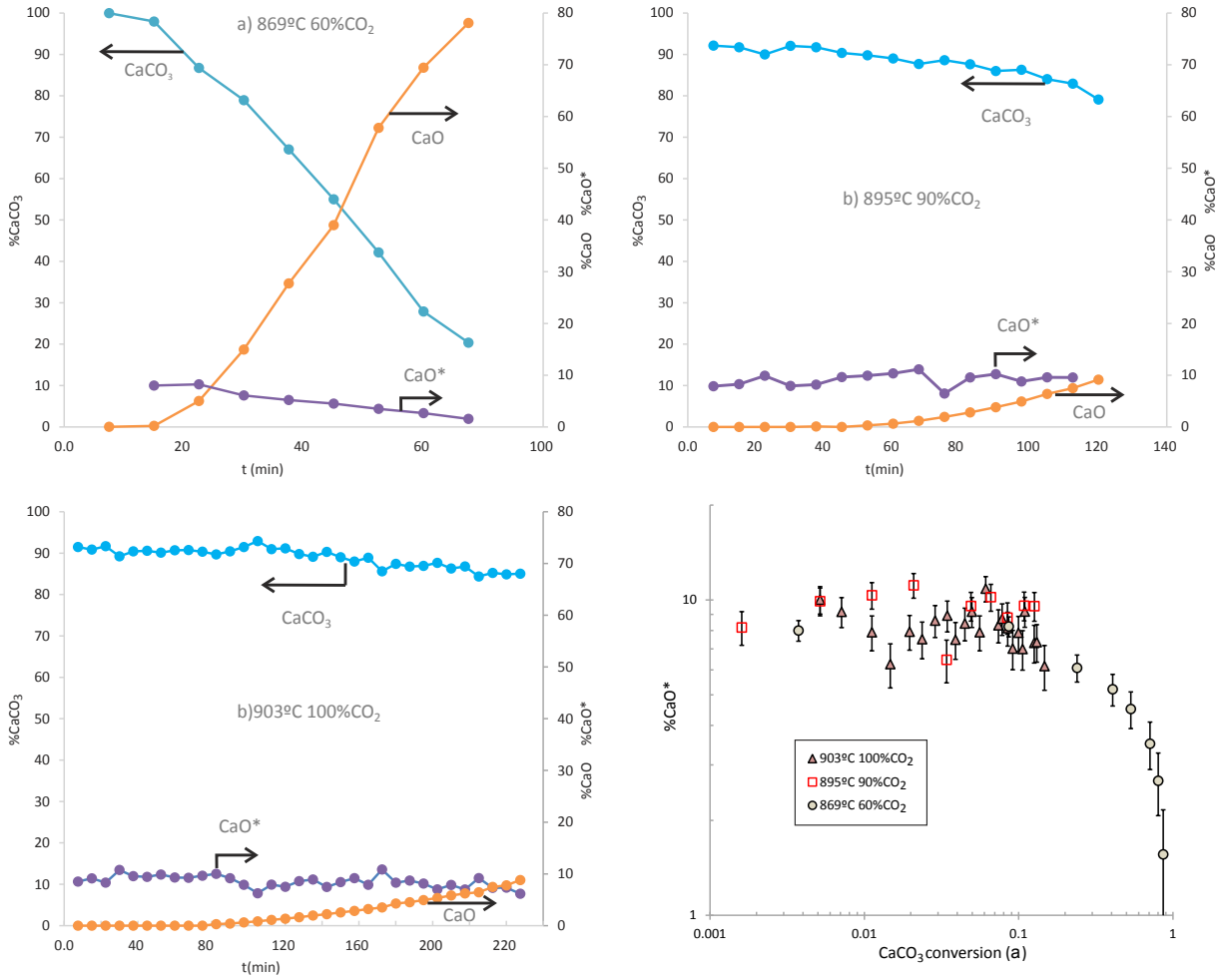

FIG. 13: a-c) Time evolution of the wt% for the three phases involved in the crystallographic transformation (calcite $CaCO_3$, CaO^* , and lime CaO) calculated by means of a Rietveld quantitative analysis for calcination tests nearby equilibrium ($P/P_{eq} = 0.9$) at the indicated conditions. d) CaO^* wt% as a function of conversion for the three calcination tests analyzed.

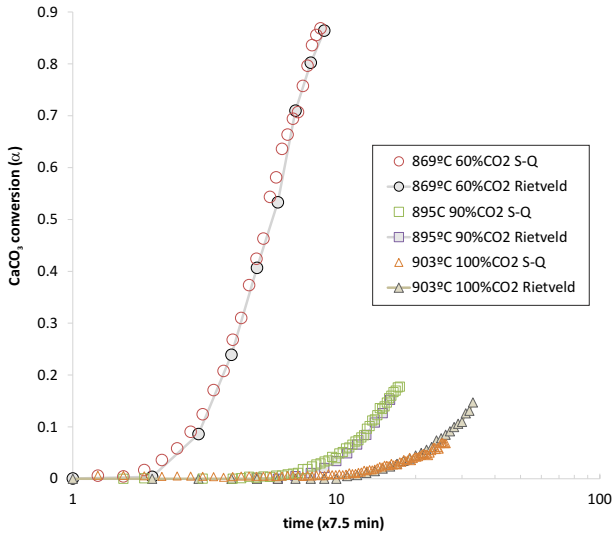

FIG. 14: Time evolution of $CaCO_3$ conversion (α) calculated from a Rietveld quantitative analysis on in-situ XRD scans registered on a wide range of diffraction angles and derived from a semi-quantitative analysis using the ratio of intensities of main $CaCO_3$ and CaO peaks in the scans registered for a reduced window of diffraction angles (Fig. 3a).